Advanced Energy Materials

ADVANCED ENERGY MATERIALS
www.advenergymat.de

RESEARCH ARTICLE OPEN ACCESS

Hybrid Two-Step Inkjet Printing and Dip-Coating Enable Scalable 30%-Efficient Perovskite/Silicon Tandem Solar Cells

Raphael Pesch[1,2] | Lena P. Rothbauer[2] | Johannes Schenk[2] | Lingyi Fang[1,2] | Theresa Kuechle[2] | Julian Petry[1] | Uma K. Dangudubiyyam[2] | Richard Thelen[1] | David B. Ritzer[2] | Ting Pan[1] | Daniel O. Baumann[1,2] | Mohammad Gholipoor[1,2] | Tonghan Zhao[1] | Nils W. Rosemann[2] | Jinzhao Li[1,2] | Ulrich Lemmer[1,2] | Ulrich W. Paetzold[1,2]

[1]Institute of Microstructure Technology (IMT), Karlsruhe Institute of Technology (KIT), Eggenstein-Leopoldshafen, Germany | [2]Light Technology Institute (LTI), Karlsruhe Institute of Technology (KIT), Karlsruhe, Germany

Correspondence: Raphael Pesch (raphael.pesch@kit.edu) | Jinzhao Li (jinzhao.li@kit.edu) | Ulrich W. Paetzold (ulrich.paetzold@kit.edu)

Received: 21 April 2026 | **Revised:** 19 August 2026 | **Accepted:** 7 September 2026

Keywords: dip-coating | inkjet printing | module | perovskite | scalability | tandem solar cell

ABSTRACT

Fully scalable fabrication routes are one cornerstone required for commercial deployment of monolithic perovskite/silicon tandem solar cells. However, to date industrially viable deposition processes delivering high performance, uniform thin films, and compatibility with established silicon manufacturing remain limited. Here, we present a fully scalable deposition strategy for the entire perovskite top-cell, including a dip-coated self-assembled monolayer hole-transport layer, a hybrid two-step inkjet-printed wide-bandgap perovskite absorber, and a dip-coated interfacial passivation. The process shows excellent reproducibility and high device performance. When integrated with textured silicon bottom cells, the tandem solar cells achieve power conversion efficiencies exceeding 30%, highlighting the technological potential of this fabrication route. Scaling the perovskite active area by a factor of >120 results in a single-junction module with an area of 12.96 cm^2 and an efficiency of 17.8%, corresponding to a loss of only 0.53%$_{abs.}$ per decade of area scaling. This highlights that our process not only delivers high performance tandem devices, but also offers excellent prospects for upscaling the device area. Extensive material analysis and device analysis substantiate the scalability, film quality, and interfacial control achieved. Importantly, this work provides the first demonstration of perovskite/silicon tandem solar cells surpassing 30% efficiency using an inkjet-printing-based perovskite absorber deposition.

1 | Introduction

Scaling up perovskite solar cell production while simultaneously maximizing material yield remains a key challenge for translating perovskite/silicon tandem solar cells (PSTs) into industrial application [1–3]. Although a variety of scalable deposition methods for perovskite thin films, such as evaporation, slot-die coating, blade coating, inkjet printing, and spray coating, have been demonstrated and shown to yield high power conversion efficiencies (PCEs), most reported devices in academic literature still rely on non-scalable processing steps. In particular, spin-coating is frequently employed during perovskite passivation or self-assembled monolayer (SAM)-based hole transport layer (HTL) deposition, preventing fully scalable device fabrication [4–13]. One reason for this reliance on spin-coating is that current most efficient PSTs (> 31% PCE) are mainly fabricated on small-area devices (1 cm^2), where spin-coating is favored due to its simplicity, rapid processing, excellent uniformity, and ability

to promote homogeneous nucleation [14]. Consequently, spin-coated SAM-based HTLs and spin-coated passivation strategies remain the dominant approaches for achieving record efficiencies at the laboratory scale [15–18]. In contrast, several studies explore scalable HTL deposition techniques, including sputtering (often still combined with spin-coated SAMs) and evaporation [7, 19]. Similarly, evaporated passivation layers based on inorganic and organic materials, such as lithium fluoride (LiF) or ethane-1,2-diammonium iodide (EDAI), have been investigated [20, 21]. However, devices fabricated using scalable approaches still exhibit lower PCEs compared to non-scalable fabricated counterparts, particularly at the small-area level. One promising and cost-effective route for the deposition of functional thin films at industrial scale is wet immersion coating, commonly referred to as dip-coating at the laboratory scale [22]. Because SAMs and passivation layers are required only in small quantities, ranging from monolayers to films a few nanometers thick, dip-coating represents an attractive, inherently scalable alternative that enables straightforward transfer of established spin-coating-based protocols. Owing to their ability to self-assemble via phosphonic acid anchoring groups, SAMs are particularly well suited for dip-coating deposition [23, 24]. The phosphonic acid linker reacts with the underlying substrate (e.g., indium tin oxide (ITO) or nickel oxide (NiO_x)), while the formation of additional layers is intrinsically suppressed, as the linker does not react with an already formed SAM [25, 26]. Indeed, the first SAM-based perovskite solar cells were demonstrated using dip-coating as early as 2018 by Magomedov et al. [27]. Despite this early demonstration, systematic investigations into the influence of dip-coating parameters, such as solution molarity, immersion time, and solution reusability, remain scarce. Even fewer studies address the replacement of spin-coated passivation layers with dip-coated alternatives. In response, this work demonstrates that both spin-coated SAM and passivation deposition can be fully replaced by a simple, fast, and scalable dip-coating process within a fully scalable PSTs fabrication process. In recent years, hybrid two-step deposition has emerged as a promising fabrication for perovskite thin films, offering significant potential for scalable PST manufacturing. Here, inorganic precursors are typically deposited in a first step via thermal evaporation, followed by the deposition of organic precursors from solution in a second step. While most studies on hybrid two-step deposition rely on non-scalable techniques such as spin-coating in the second step, PSTs fabricated using this fabrication route have already achieved PCEs exceeding 33% [17, 18, 28]. By integrating the advantages of both deposition methods, namely, the conformal and highly controlled film formation enabled by evaporation, and the rapid, low-cost processing afforded by solution-based deposition, this hybrid strategy enables the formation of uniform, large-area thin films. Importantly, it also shows compatibility with industrial requirements, including deposition on textured silicon substrates [29]. Here, using a hybrid two-step inkjet-printing approach, combining evaporation of all inorganic perovskite precursor materials with scalable inkjet printing of all organic precursor materials, we deposit the perovskite absorber entirely by scalable methods. All surrounding layers are likewise fabricated using industrially compatible processes, including evaporation and atomic layer deposition for the electron transport layer, sputtering for the transparent conductive oxide, and evaporation for the electrodes. We present a detailed deposition protocol identifying critical dip-coating parameters, including solution molarity, dip-coating time, and material yield enabled by repeated solution reuse, and elucidate how these parameters affect device performance. All dip-coated devices are benchmarked against an optimized spin-coating-based reference, demonstrating that dip-coating does not impose a performance penalty. A champion wide-bandgap single-junction perovskite solar cell (PSC) reaches a PCE of 20.1%. Finally, the here optimized dip-coating based SAM and passivation deposition is used to fabricate a perovskite mini-module with an active area of 12.96 cm^2 that even though being 123 times larger than the PSCs used for optimization, shows an only 0.53%$_{abs.}$ loss in PCE per decade of area scaling with an absolute PCE of 17.8%. Additionally textured PSTs are fabricated reaching a single scan champion PCE of up to 30.2% (30% during 10-min MPP tracking), which to the best of our knowledge is the highest reported PCE for a PST fabricated using an inkjet printing step to deposit the perovskite.

By combining dip-coating for the perovskite-adjacent layers, namely the SAM and the passivation layer, with a hybrid two-step perovskite deposition process employing inkjet printing for precise spatial control, we demonstrate a scalable fabrication route for efficient PSTs. This approach represents an important step toward the industrialization of perovskite-based tandem photovoltaics.

2 | Results and Discussion

We present a fully scalable fabrication route for PSTs based on three complementary deposition strategies that enable uniform, high-quality thin films and, consequently, high PCEs. More precisely, the resulting PSTs achieve PCEs exceeding previously reported hybrid two-step processed PSTs employing scalable perovskite deposition, while extending scalability to all other functional layers within the device stack [30]. Furthermore, for the first time, such PCEs are achieved using an inkjet-printing-based perovskite fabrication route. The process begins with the formation of the HTL, comprising a SAM, deposited via a highly reproducible dip-coating method (Figure 1a). We systematically investigate the influence of solution molarity and immersion time, including material utilization across consecutive fabrication cycles, achieving device performance comparable to an optimized spin-coating reference while improving scalability. The perovskite absorber is then formed via a hybrid two-step approach, starting with vapor-phase deposition of the inorganic perovskite precursors (Figure 1b), followed by inkjet printing of the organic precursors to complete conversion with precise spatial control (Figure 1c). After crystallization, a widely used passivation layer based on propane-1,3-diammonium iodide ($PDAI_2$) and n-butylammonium iodide (BAI) is applied by dip-coating (Figure 1d), with processing parameters again systematically evaluated [30–32]. Finally, the scalability of the developed fabrication route is demonstrated by fabricating a highly efficient wide-bandgap perovskite mini-module suitable for tandem integration, as well as monolithic PSTs achieving a record PCE exceeding 30% for inkjet-printed perovskite deposition. The complete device architecture, including electron transport layer, electrodes, and anti-reflection coating, is shown in Figure S1.

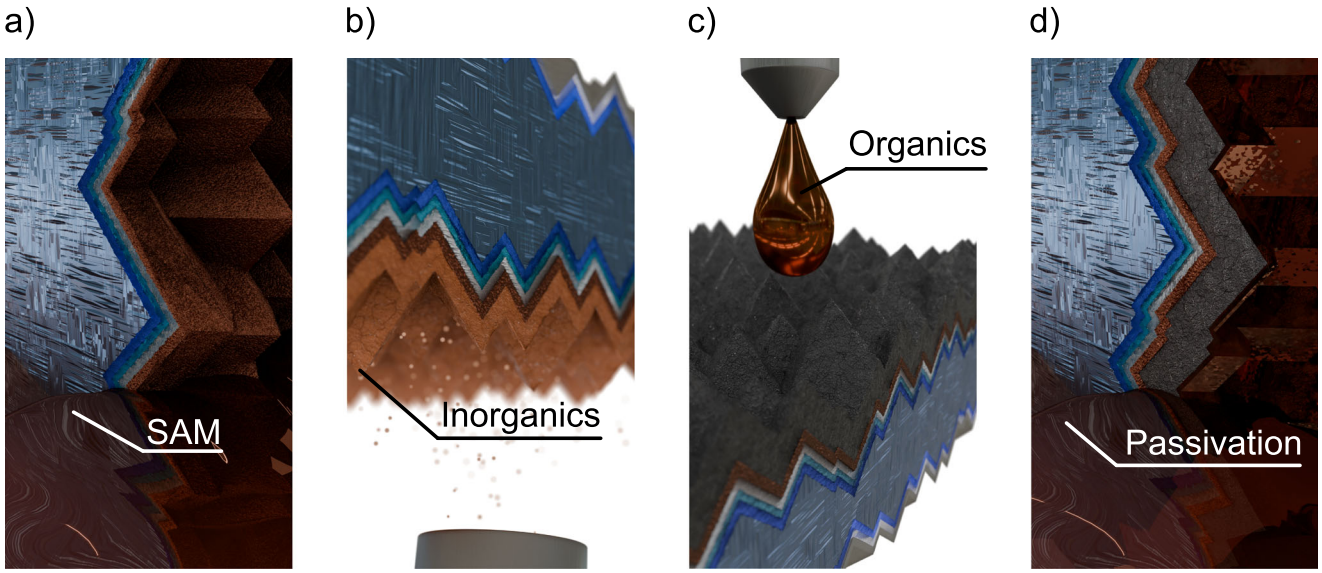

FIGURE 1 | Fully scalable fabrication process of a perovskite thin film and its surrounding thin films on top of a textured heterojunction silicon solar cell using (a) dip-coating for the self-assembled monolayer, (b) evaporation for the inorganic precursor materials, (c) inkjet printing for the organic precursor materials, and (d) dip-coating for the passivation.

2.1 | Scalable HTL Deposition Using Dip-Coating

In the following, we demonstrate scalable dip-coating deposition of SAMs provides excellent wetting and compatible performance to spin-coated counterparts. Dip-coating yields a higher open-circuit voltage (V_{OC}), improved SAM coverage, and strongly reduced material waste compared with spin-coating. By optimizing SAM molarity and immersion time, we fabricate ~1.68 eV wide-bandgap PSCs with performance on-par with that of optimized spin-coated references. SAM-based PSCs are first reported in 2018 by Magomedov et al., while Al Ashouri et al. introduce the second generation of SAMs, including 2PACz used in this work, in 2019 [27, 33]. Both studies investigate dip-coating and spin-coating as deposition methods and obtain similar device performance. However, the process window with respect to molarity, immersion time, and solution lifetime remains largely unexplored. Here, we address this gap using a fully scalable perovskite deposition process based on hybrid two-step inkjet printing, first introduced by our group in 2024 for single-junction PSCs and in 2025 for PSTs [34, 35]. For all single-junction PSCs, we use 2PACz as the SAM. As demonstrated in PST fabrication, the SAM molecule can be replaced, for example, by (4-(3,6-diphenyl-9H-carbazol-9-yl) butyl)phosphonic acid (Ph4PACz). As a reference for the dip-coated PSCs, we employ an optimized process from our previous work using a 0.5 mg mL^{-1} spin-coated 2PACz HTL, corresponding to 1.82 mM. These reference PSCs show a median PCE of 18.5%, with a FF of 80%, a V_{OC} of 1.16 V (Figure 2a–c), and a current density (J_{SC}) of 19.9 mA cm^{-2} (Figure S2). By increasing the SAM molarity during dip-coating from 0.015 mg mL^{-1} (≈ 0.055 mM) to 1.5 mg mL^{-1} (≈ 5.500 mM), we observe a clear correlation with device performance. PSCs fabricated with 0.055 mM exhibit a low median PCE of 14.5% and a standard deviation of 1.5%, which originates from a reduced median FF of 67% and a large standard deviation in V_{OC}. In contrast, PSCs fabricated with SAM molarities ≥ 0.27 mM show strongly improved PCE and reduced standard deviations of 0.2%–0.5% (excluding outliers), as shown in Figure 2a–c. We therefore identify 0.27 mM as the minimum SAM molarity required for reproducible PSC performance. Further increasing the SAM molarity to 0.550 and 5.500 mM results in median PCEs of 18.0% and 18.2%, respectively, matching the performance of spin-coated references. Notably, the V_{OC} of all dip-coated PSCs fabricated with molarities ≥ 0.27 mM exceeds that of spin-coated devices. Moreover, V_{OC} increases monotonically with increasing SAM molarity and reaches a median value of 1.19 V at 5.500 mM (Figure 2c). Analysis of J_{SC} and EQE attributes these trends to differences in SAM coverage. Spin-coated PSCs show median J_{SC} values of 19.9 mA cm^{-2} and EQE values exceeding 80% between 400 and 700 nm, indicating efficient charge extraction. In contrast, PSCs fabricated with 0.055 mM SAM exhibit an overall EQE reduction of 5%, consistent with inefficient charge extraction caused by incomplete SAM coverage (Figure 2d and Figure S2). Increasing the molarity to 0.27 mM and 0.550 mM raises the EQE to values comparable to spin-coated PSCs. At 5.500 mM, the EQE decreases by 5% in the 400–500 nm range while remaining comparable at longer wavelengths (Figure 2d). This suggests reduced hole extraction at the HTL side, since shorter wavelengths are absorbed closer to the p-side in p-i-n PSCs. We hypothesize, that increased SAM density slightly limits charge extraction, but simultaneously reduces interfacial trap-states, boosting the V_{OC} and FF. X-ray photoelectron spectroscopy (XPS) reveals an increase in SAM coverage with increasing 2PACz solution molarity from 0.055 to 5.500 mM. Notably, the SAM coverage obtained by dip-coating from a 5.500 mM solution exceeds that of the spin-coated reference sample (Figure S3a). Quantitatively, the phosphorus-to-indium ratio (used as a measure of SAM coverage) increases from 13.09% for the 0.055 mM sample to 13.49% for the spin-coated reference and further to 17.67% for the 5.500 mM sample (Figure S3b). Ultraviolet photoelectron spectroscopy (UPS) is employed to investigate changes in energy-level alignment (Figure S4). For

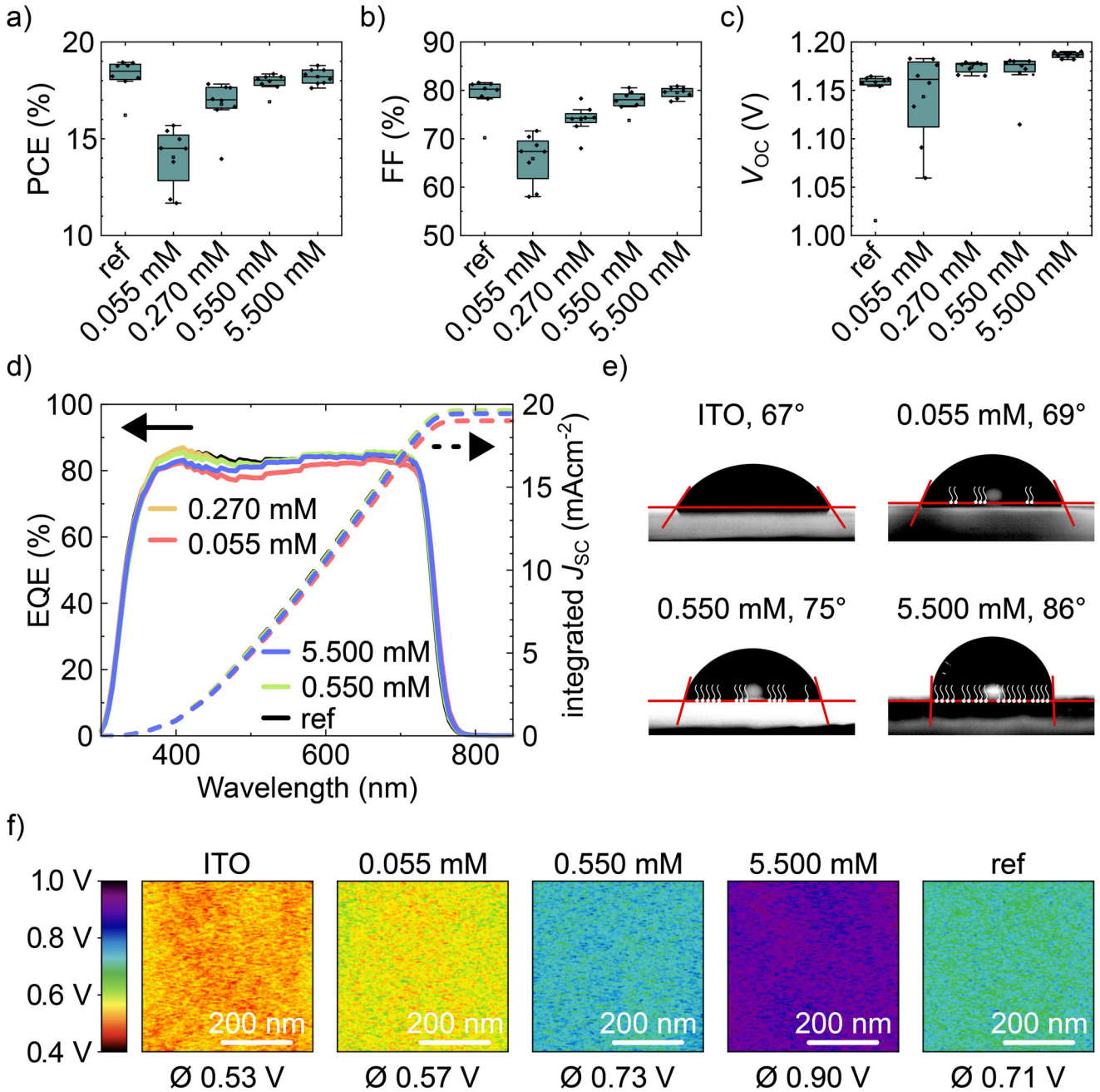

FIGURE 2 | Comparison between perovskite solar cells fabricated by spin-coating the 2PACz (ref) self-assembled monolayer versus applying it using different molarities during dip-coating, investigating (a) the power conversion efficiency, (b) the fill factor, (c) the open-circuit voltage, and (d) the external quantum efficiency. (e) ITO surfaces covered with and without the differently deposited 2PACz self-assembled monolayers are investigated using optical contact angle measurements using water and f) Kelvin probe force microscopy.

the 0.055 mM sample, the Fermi level is separated from the valence band maximum by 0.90 eV. Increasing the molarity to 5.500 mM improves the band alignment, reducing this energy offset to 0.67 eV. However, despite the higher SAM coverage achieved at 5.500 mM, the spin-coated reference exhibits a slightly more favorable band alignment. This observation suggests that the small reduction in J_{SC} observed at 5.500 mM may partially originate from less efficient charge extraction caused by the slightly inferior energy-level alignment. At the same time, both the FF and V_{OC} continue to increase, indicating that these parameters are strongly influenced by the enhanced SAM coverage and increased interfacial passivation. This interpretation agrees with observations reported by Yeddu et al. and Qu et al. [36, 37]. Optical contact-angle measurements further support this hypothesis. With decreasing SAM molarity, the contact angle approaches that of pristine ITO (~ 67°). Substrates dip-coated using 5.500 mM show a median contact angle of 86°, which decreases to 75° for 0.550 mM and to 69° for 0.055 mM (Figure 2e). This trend indicates reduced SAM coverage at lower molarities, allowing stronger interaction between the water droplet and exposed ITO regions. We further investigate SAM coverage using Kelvin probe force

microscopy (KPFM) on glass/ITO substrates coated with 2PACz by spin-coating and dip-coating. Pristine ITO exhibits a surface potential of 0.53 V. For dip-coated SAMs, the surface potential increases from 0.57 V at 0.055 mM to 0.73 V at 0.550 mM and to 0.90 V at 5.500 mM (Figure 2f), while spin-coated SAMs show 0.71 V. These results further confirm that higher SAM molarity produces a more compact and complete monolayer. Using a 0.550 mM 2PACz solution, we study the influence of dip-coating time by comparing durations of 6, 60, and 600 s. Neither shorter nor longer immersion times improve device performance (Figure S5a–d). Extended immersion times yield comparable results, whereas very short immersion times increase the FF standard deviation to 3.5% (excluding outliers; Figure S5b). Because SAMs form monolayers, dip-coating consumes only negligible amounts of 2PACz. We therefore examine solution reuse by fabricating 70 substrates in ten dip-coating runs (seven substrates per run). The first 35 substrates are processed immediately, while the remaining 35 are fabricated one month later using the same solution stored in a nitrogen-filled glovebox. We observe neither run-dependent nor time-dependent degradation in PCE, demonstrating that the dip-coating solution remains usable for at least one month. This result strongly enhances material utilization compared with spin-coating (Figure S6a,b).

2.2 | Scalable Passivation Using Dip-Coating

Next, we introduce dip-coating as an alternative deposition method for the often-used solvent-based passivation $PDAI_2$, enabling lossless scaling with reduced PCE variability [30–32]. Namely, we evaluate the influence of solution molarity and immersion time. To assess the replacement of spin-coating, PSC passivated using dip-coating are compared with the reference PSCs described above and fabricated according to our previously reported process [35]. The reference passivation uses a solution containing 1 mg mL^{-1} $PDAI_2$ and 1 mg mL^{-1} BAI in IPA (≈ 5 mM total concentration). For dip-coating, we investigate significantly lower concentrations: 240.0, 24.0, and 2.4 µM. Despite the much lower molarity, and therefore substantially improved material efficiency, the champion devices exhibit PCE values on par with the spin-coated reference (Figure 3a). However, PSC performance strongly depends on the chosen concentration and must be carefully optimized. At 24.0 µM, devices achieve a median FF of 80.4%, whereas increasing the concentration to 240.0 µM broadens the performance distribution and reduces the median FF to 78.4% (Figure 3b). Reducing the concentration to 2.4 µM also lowers the FF (78.3%) and decreases V_{OC}, which we attribute to insufficient passivation and remaining surface defects (Figure S7a). Devices passivated at 24.0 µM show very low absolute hysteresis (1%), comparable to spin-coated samples (Figure 3c). In contrast, both lower and higher concentrations increase hysteresis toward 3%. J_{SC} and integrated J_{SC} confirm efficient conversion and charge extraction for both deposition methods, while higher concentrations (240.0 µM) slightly reduce the EQE by 1%–2%, suggesting marginally hindered charge extraction (Figure 3d and Figure S7b). To further assess the optoelectronic quality of the perovskite thin films, time-resolved photoluminescence (TRPL) measurements are performed using time-correlated single-photon counting (TCSPC). The results reveal a trend that is consistent with the observed PSC performance. Perovskite thin films with spin-coated passivation exhibit the longest charge-carrier lifetimes, while comparable lifetimes are observed only for thin films passivated by dip-coating in a 24 µM solution (Figure 3e and Figure S8). Increasing or decreasing the dip-coating precursor concentration results in a pronounced reduction in carrier lifetime. This reduction is attributed to additional non-radiative recombination pathways arising from an incomplete passivation layer at 2.4 µM and an excessively thick passivation layer at 240 µM, respectively [38]. UPS measurements show that spin-coated passivation and dip-coated passivation at 24 µM induce a similar shift of the conduction-band minimum toward the Fermi level. This shift is slightly more pronounced for the spin-coated samples, which may account for the 0.01 V higher median V_{OC} achieved using this deposition method (Figures S7a and S9). XPS analysis of the N 1*s* and Pb 4*f* regions reveals similar trends for both passivation methods, despite the approximately two-orders-of-magnitude lower precursor concentration used for dip-coating. In the N 1*s* region, comparable peak broadening is observed for the spin-coated and 24 µM dip-coated samples, indicating overlapping contributions from the N 1*s* orbitals of PDA^+ and BA^+ and those of the FA^+ and MA^+ orbitals of the perovskite (Figure S10a). Consistent with this interpretation, perovskite thin films passivated by dip-coating at the lower concentration of 2.4 µM exhibit less pronounced N 1*s* peak broadening. Similarly, the Pb 4*f* peaks shift toward lower binding energies for both samples passivated by spin-coating and by dip-coating at 24 µM (Figure S10b). This shift indicates effective surface passivation and a pronounced interaction between the passivation molecules and the perovskite surface [15, 30]. By comparison, the 2.4 µM dip-coated sample exhibits a less pronounced shift, further supporting the conclusion that this concentration results in insufficient passivation. We attribute the comparable passivation achieved despite the approximately two-orders-of-magnitude difference in precursor concentration to the distinct deposition dynamics. During dip-coating, the prolonged immersion of the perovskite film in the precursor solution likely compensates for the lower concentration, whereas during spin-coating, the perovskite thin film is exposed only briefly to a more concentrated solution before it is rapidly expelled at 4000 rpm. Next, using k-mapping, we analyze the spatial distribution of recombination properties [39]. Spin-coated thin films show a homogeneous distribution with a mean k-value of 1.42 (Figure 3f). Dip-coated films processed at 24.0 µM exhibit faint drying patterns that originate from drying of the fully wetted substrate on the hotplate, likely caused by the current laboratory-scale setup, which does not completely remove residual solvent before annealing. Gradually increasing the annealing temperature did not eliminate these drying-induced effects. However, N_2-gas-flow-assisted drying prior to annealing provides a suitable approach to mitigate them (Figure S11a–c). Nevertheless, despite the observed local variations, device statistics remain highly uniform: the standard deviation in V_{OC} is only 1.94 mV for dip-coated devices, compared with 3.49 mV for spin-coated counterparts (excluding one shunted cell). Using the optimized concentration of 24.0 µM, we next vary the immersion time (6 s, 60 s, and 600 s). A duration of 60 s delivers the best median performance across all photovoltaic parameters (Figure S12a–d). Shorter (6 s) and longer (600 s) treatments slightly reduce V_{OC} by 10 mV and FF by 1–2%, yet still yield median PCE values around 18%, revealing a broad and robust processing window. Finally, we combine the optimized conditions for both interlayers,

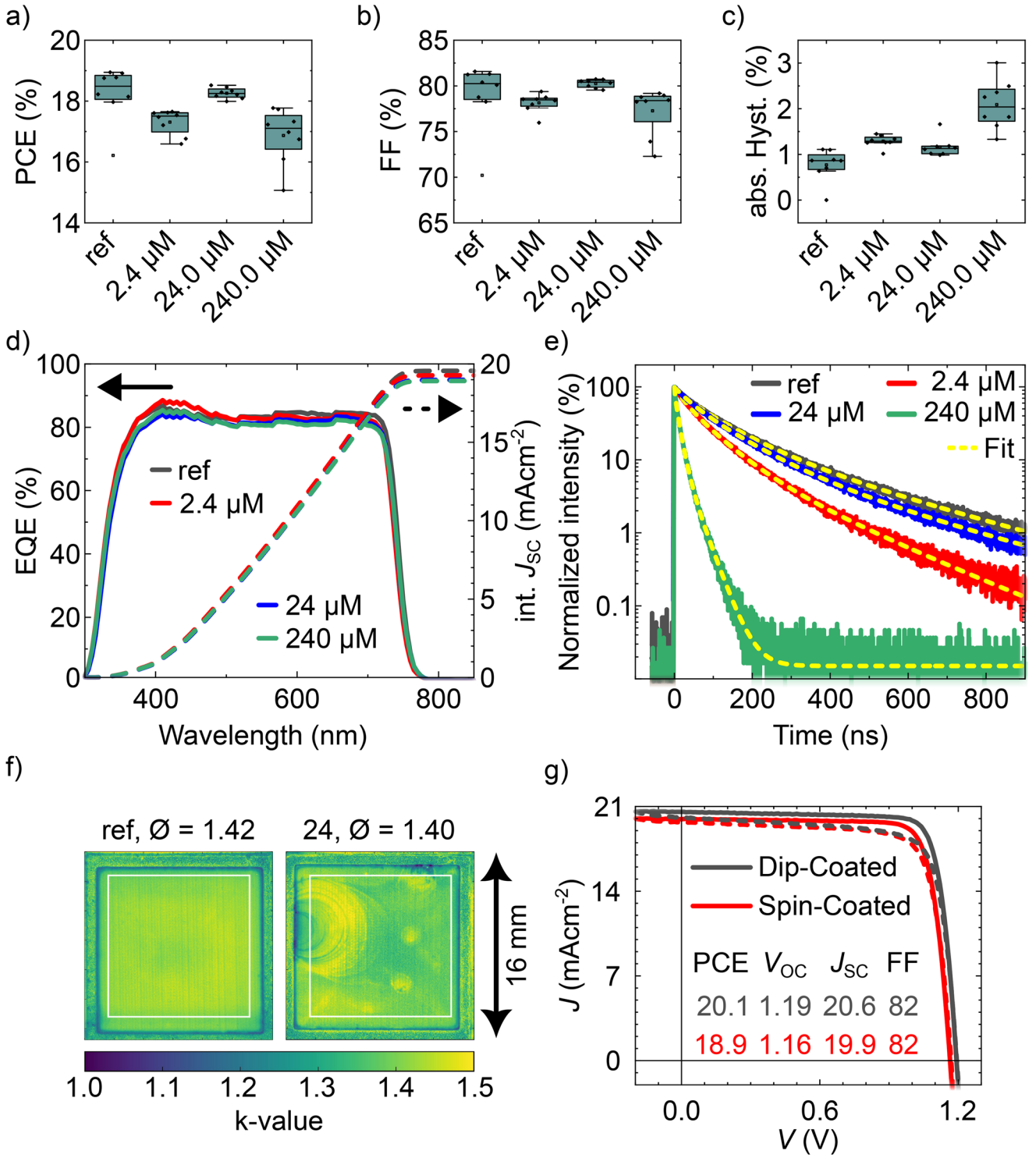

FIGURE 3 | (a) Power conversion efficiency, (b) fill factor, (c) absolute hysteresis, (d) external quantum efficiency, and (e) time-resolved photoluminescence (TRPL) measurements of the perovskite thin films passivated using spin-coating (ref) and different molarities while dip-coating (2.4, 24.0, and 240.0 µM). (f) k-maps of a perovskite thin film passivated using spin-coating (ref) and the best performing dip-coating molarity (24.0 µM). (g) *JV*-curves of the champion perovskite solar cells fabricated using spin-coating for the self-assembled monolayer and passivation, as well as using dip-coating for both.

SAM deposition at 5.500 mM for 60 s and passivation at 24.0 µM for 60 s, to fabricate a batch of wide-bandgap PSCs. These PSCs achieve a champion PCE of 20.1% with a median of 18.9%, enabled by a median V_{OC} of 1.19 V, median J_{SC} of 19.7 mA cm^{-2}, and median FF of 80% (Figure 3g and Figure S13a–d). EQE of the champion PSC confirms sufficient conversion with an integrated J_{SC} of 20.4 mA cm^{-2} (Figure S14). To the best of our knowledge, these results represent the highest efficiencies reported for wide-bandgap PSCs fabricated using an inkjet-printed perovskite deposition step.

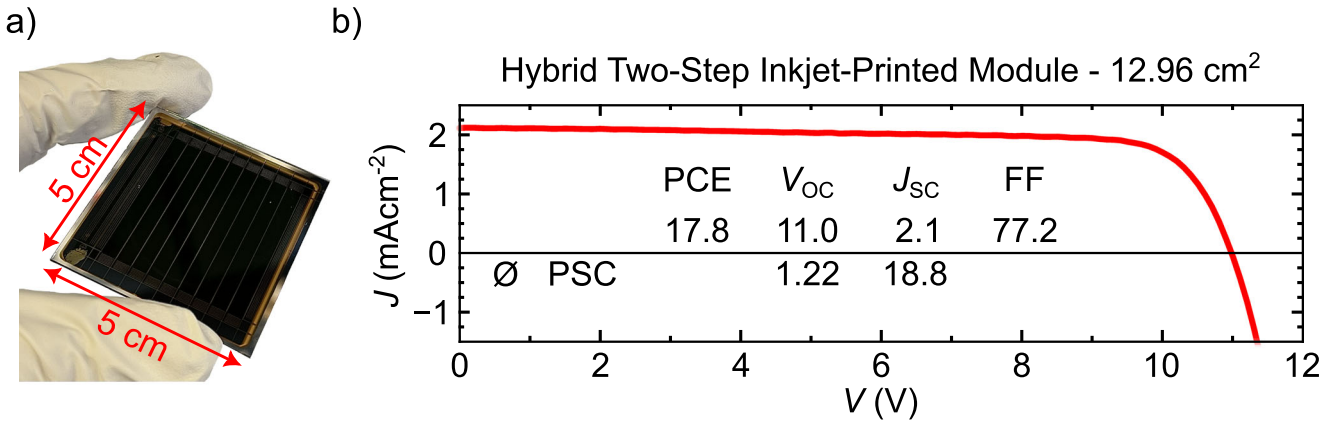

FIGURE 4 | (a) Photograph and (b) *JV*-curve of the 12.96 cm^2 (aperture area) wide-bandgap perovskite mini-module consisting of nine perovskite solar cell stripes.

2.3 | Large Area Deposition Enabling Module Integration

Although several studies report hybrid two-step fabricated PSC modules, this work is, to the best of our knowledge, the first to demonstrate a wide-bandgap PSC module using this deposition method. In 2022, Tan et al. report a remarkable PCE of 23.7% for PSCs with an active area of 1 cm^2. Upon scaling the active area to 4×4 cm^2, the PCE decreases to 20.02%, corresponding to a 3.06% absolute loss per decade in area scaling. It should be noted that a medium-bandgap absorber in an n–i–p architecture is employed, which is not suitable for tandem integration. Furthermore, spin-coating is used for the deposition of the organic precursors, inherently limiting the scalability of the process. As already evident from a photograph of the perovskite thin film, spin-coating artifacts are visible to the naked eye [40]. Similar artifacts are reported using electroluminescence imaging by Pisoni et al., who fabricate a flexible module with an active area of 9.6 cm^2 consisting of eight serially interconnected sub-cells. Their hybrid two-step process also combines thermal evaporation and spin-coating within an n–i–p architecture. Despite the challenges associated with flexible substrates, the module achieves a notable PCE of 10.5%. However, they report an absolute loss per decade in area scaling of 2.38%, since their small-area PSCs (0.15 cm^2), reaches a PCE of 14.8% [41]. In contrast, the photograph of the PSC fabricated in this study (Figure 4a) shows homogeneous thin-film formation across the entire coated area, enabled by inkjet printing, highlighting the compatibility of the process with scalable manufacturing. Recently, Yu et al. report large-area perovskite thin films fabricated via a hybrid two-step process combining evaporation and blade-coating. Although their modules exhibit a substantial active area of 8×8 cm^2, device performance is limited by shunting, resulting in a FF of only 64% and a PCE of 12.6%. In addition, a bandgap of 1.55 eV is employed, which is not optimal for tandem applications [42]. In this work, dip-coating is used for the deposition of the 2PACz SAM-HTL and for interfacial passivation, in combination with hybrid two-step inkjet printing for perovskite deposition. This approach enables a fully scalable module fabrication route. Moreover, a p–i–n architecture is implemented, demonstrating the suitability of the developed process for tandem integration. For module fabrication, a 5×5 cm^2 glass/ITO substrate is coated, of which a central region of 3.6×3.6 cm^2 (12.96 cm^2) serves as the active area. The module layout is defined by laser scribing, forming nine serially interconnected sub-cells, each with an active area of 1.44 cm^2. The optimized recipes for SAM formation and perovskite/ETL passivation developed above are directly transferred to the module process using dip-coating. The resulting mini-module achieves a PCE of 17.8%, corresponding to an absolute efficiency loss of 1.1% per decade of area scaling considering the champion small-area PSC. When compared to the median PCE of small-area devices, the loss is only 0.53% absolute per decade of area scaling (Figure 4b). The measured V_{OC} of 10.97 V indicates a high yield of well-performing sub-cells. Nevertheless, the mini-module still exhibits considerable potential for further reduction of upscaling-related losses. It should be noted that one of the main contributors to the observed scaling losses is the custom-built laser scribing setup employed in this work. The limited precision of the system can lead to reduced shunt resistance due to imperfect scribing. Furthermore, during the P3 scribing process, the ablated silver is not always completely removed but can instead be partially fractured and redistributed, resulting in local shunting of individual sub-cell regions (Figure S15). Notably, the lowest area-dependent PCE losses achieved in-house with the current setup have not yet been below 1% absolute per decade increase in active area [43]. We therefore attribute a significant fraction of the observed scaling losses to the limitations of the laser scribing process rather than to the scalable deposition methods themselves. We anticipate that the use of a more advanced and precisely controllable laser scribing system would further reduce scaling losses and enable improved mini-module performance.

2.4 | Tandem Solar Cell Integration

As a proof of concept extending beyond single-junction architectures, we apply the double dip-coating process in combination with the scalable hybrid two-step inkjet-printed perovskite deposition to textured heterojunction silicon bottom cells with a 1 cm^2 active area (Figure 5a). For these PSTs, we retain the same passivation strategy but replace the SAM 2PACz with Ph4PACz. This substitution is beneficial because Ph4PACz provides improved wettability on the textured silicon surface. In addition, Ph4PACz

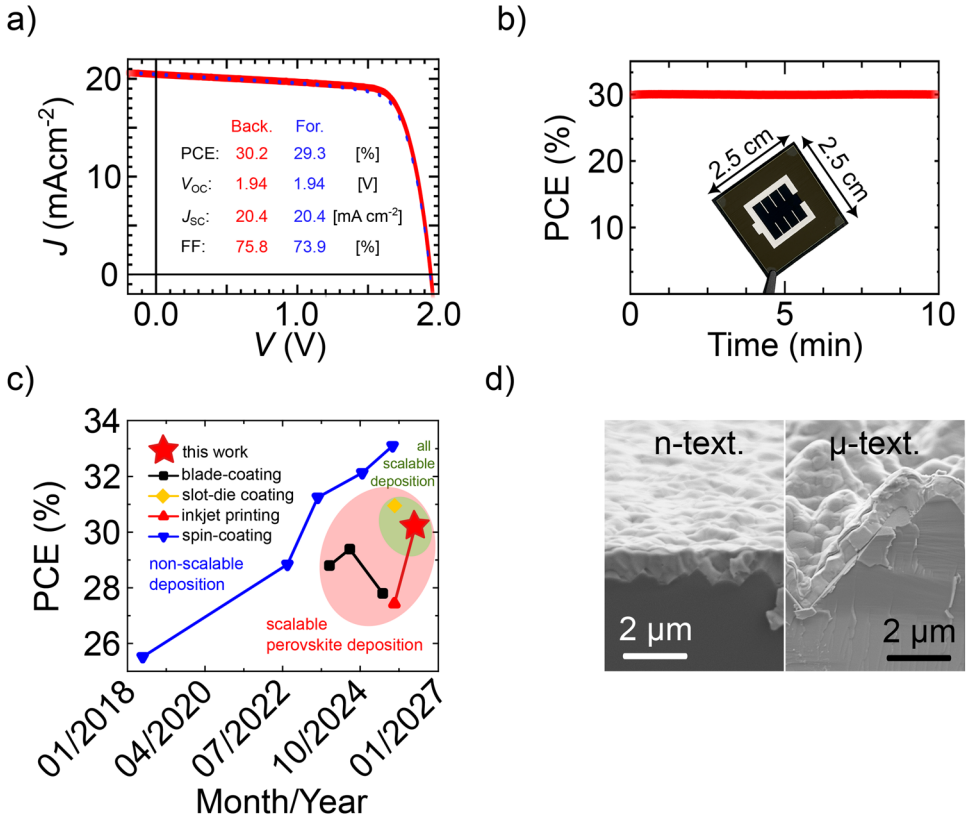

FIGURE 5 | (a) *JV*-curve of the champion perovskite/silicon tandem solar cell. (b) Photograph, together with maximum power point tracking over 10 min. (c) Comparison of champion perovskite/silicon tandem solar cells fabricated using hybrid two-step deposition. (d) Scanning electron microscopy image of the tilted cross-section of the perovskite thin film deposited on nano- and micron-textured silicon bottom cells.

is reported to enable high V_{OC} and FF due to improved band alignment and reduced interfacial energy losses [44]. Consistent with previous observations for 2PACz on planar glass/ITO substrates, dip-coating Ph4PACz from a 5.500 mM methanolic solution onto textured silicon substrates produces a denser and more robust SAM. KPFM reveals a surface potential 0.06 V higher than that of the spin-coated reference and 0.19 V higher than that of substrates coated with pristine NiO_x (Figure S16). In agreement with these findings, XPS shows an increase in both the #P signal intensity and the #P/#Ni ratio, which serves as an indicator of SAM density. Specifically, the #P/#Ni ratio increases from 9.1% for the spin-coated substrates to 20.1% for the dip-coated substrates (Figure S17a,b). Finally, ultraviolet photoelectron spectroscopy (UPS) indicates slightly improved energy-level alignment for the dip-coated SAMs (Figure S18). Using this fully scalable interlayer deposition approach, the champion PST reaches a PCE of 30.2%, enabled by a V_{OC} of 1.94 V, a J_{SC} of 20.4 mA cm^{-2} (> 20 mA cm^{-2} according to EQE), and a FF of 75.8% (Figure 5a and Figure S19). To our knowledge, this constitutes the first report of an inkjet printing-based perovskite deposition to fabricate PSTs surpassing the 30% efficiency threshold and, consequently, the highest efficiency achieved for a PST fabricated from an inkjet printing-based perovskite precursor. While several studies have reported PSTs with PCEs of 28%–30% fabricated via hybrid two-step deposition using blade coating, our results position inkjet printing as a strong competitor (Figure 5c) [9, 45, 46]. Moreover, given that only a single study has so far explored slot-die coating in combination with fully scalable PSC fabrication, our work demonstrates that a transition toward fully scalable processing does not inherently compromise device performance [47]. By implementing dip-coating as a scalable alternative to spin-coated passivation, highly effective passivation molecules such as $PDAI_2$-BAI can be employed, enabling the achievement of the highest reported V_{OC} among (fully) scalable hybrid two-step fabricated PSTs (Table S1). It should be noted that, compared to the planar single-junction champion PSC, the observed reduction in FF is primarily attributed to the not fully optimized tandem architecture on the textured substrate. This leads to increased series resistance and a pronounced decrease in shunt resistance. In contrast, fabrication of a planar silicon-based PST yields a substantially higher FF of 78%, albeit at the expense of a reduced J_{SC} due to the reduced light management capabilities (Figure S20). Even though the textured PST exhibits a reduced FF, it sustains a PCE above 30% during 10 min maximum power point tracking and exhibits a t_{80} lifetime of 100 h (Figure 5b,c and Figure S21). Notably, this lifetime, achieved without encapsulation, is twice that of our previously reported hybrid two-step inkjet-printed PSTs [35]. Compared to our recent work using sequential evaporation, we observe no reduction in stability when moving from non-scalable fabrication to fully scalable processing on texture. This highlights robust SAM-HTL formation even on textured substrates [48]. Compared with published champion PSTs exceeding 33% PCE, which are fabricated using non-scalable one-step spin-coating or a hybrid two-step deposition, devices based on the latter method continue to exhibit limited long-term stability [18, 49]. Similarly, in the present study, t_{80} lifetimes exceeding 100 h are not achieved. As shown in our previous work, PST degradation

is primarily associated with decreases in J_{SC} and FF, whereas V_{OC} remains largely unaffected [35]. Thiesbrummel et al. reported that this degradation trend is indicative of electric-field screening induced by mobile ions under prolonged illumination, which in the present study is applied under ISOS-L1 conditions [50, 51]. Assuming that degradation of the perovskite absorber is the dominant contributor to the overall device degradation, we investigated whether dip-coating both the SAM-based HTL and the molecular passivation layer limits PSC stability. For this purpose, long-term MPP-tracking is performed on one-step spin-coated PSCs fabricated according to the procedure reported by Fang et al. [15]. Based on the published perovskite formulation, wide-bandgap PSCs are fabricated and tracked for 420 h. Both PSC types exhibited similar light-induced degradation behavior. As shown in Figure S22, the dip-coated PSCs showed a slightly improved stability (t_{80} = 356 h) than the spin-coated reference PSCs (t_{80} = 309 h). It should be noted that the optimized passivator concentration reported by Fang et al. is used for the spin-coated passivation layer. In contrast, the dip-coating conditions are not reoptimized. Instead, a concentration of 24 µM and a deposition time of 60 s is applied. Beyond the champion PSTs, the scalable fabrication process demonstrated good batch-to-batch reproducibility, achieving a median PCE of 29.5% across four tandem solar cells fabricated in four independent consecutive batches (Figure S23a). The high median V_{OC} of 1.93 V, together with a median J_{SC} value exceeding 20 mA cm^{-2} and a moderate median absolute hysteresis < 1% (Figure S23b–e), indicates excellent HTL formation and effective surface passivation, enabled by replacing all spin-coating steps by dip-coating. It should be noted that, due to design constraints of the evaporation system, only three PSTs can be fabricated per batch during the inorganic precursor deposition step. To ensure near-optimal stoichiometry, one PST is printed at the nominal resolution, while the remaining two PSTs are printed at resolutions of ±80 DPI. This strategy compensates for minor batch-to-batch variations in the deposited material quantity without requiring in-line process monitoring. Although industrial manufacturing would rely on advanced process control to maximize device yield and ensure uniform product quality, the present approach is chosen to demonstrate the feasibility and performance potential of the hybrid two-step inkjet-printing process. Consequently, an effective device yield of approximately 33% is accepted within this research-scale study. For completeness, the PCE evolution of all PSTs fabricated across four consecutive batches is presented in Figure S24. Lastly, the developed inkjet-printing-based hybrid two-step process demonstrates excellent versatility for integration with textured tandem architectures. In our previous study, micron-textured silicon bottom cells from a different supplier were investigated [35]. In contrast, the transition to nano-textured silicon bottom cells in the present work does not require any modifications to the perovskite deposition process, apart from a 40% reduction in the amount of material deposited during both evaporation and inkjet printing. A comparison of SEM images of perovskite thin films deposited on micron- and nano-textured substrates reveals highly conformal film growth, independent of the underlying surface morphology (Figure 5d). Additionally, Grazing-Incidence Wide-Angle X-ray Scattering (GIWAXS) measurements of both perovskite thin films show no discernible differences, supporting the assumption that crystallization proceeds identically regardless of the underlying texture (Figure S25a,b).

3 | Conclusions

Perovskite/silicon tandem solar cells represent one of the most promising pathways to surpass the efficiency limits of established photovoltaic technologies, provided that laboratory-scale performance can be translated into industrially viable manufacturing processes. In this work, we demonstrate a fully scalable deposition strategy for perovskite top solar cells that addresses this challenge. By replacing spin-coating with dip-coating for the deposition of self-assembled monolayer based hole-transport layers and interfacial passivation layers, we achieve perovskite solar cells with efficiencies exceeding those of optimized spin-coated references. Importantly, this approach enables the use of highly effective passivation molecules that have previously been introduced for spin-coating processes. We show that precise control over solution molarity, immersion time, and processing protocols is essential to ensure high performance and reproducibility, while the ability to reuse self-assembled monolayer dip-coating solutions across multiple batches improves material utilization and process sustainability. When extended to larger areas, the scalable deposition scheme results in a wide-bandgap perovskite module (12.96 cm^2) with a PCE of 17.8% and minimal power conversion efficiency losses of 0.53%$_{abs.}$ per decade in area scaling. Integrating these perovskite top cells with textured silicon bottom cells yields fully scalable perovskite/silicon tandem solar cells, fabricated using dip-coating for critical interfaces and a hybrid two-step inkjet printing process for the perovskite absorber. This approach achieves power conversion efficiencies exceeding 30% with stable operation (t_{80} = 100 h). To the best of our knowledge, this is the first demonstration of perovskite/silicon tandem solar cells surpassing 30% efficiency that incorporate an inkjet printing step in the perovskite deposition process. These results underscore the potential of combining dip-coating and inkjet printing as industrially compatible fabrication routes, marking a significant step toward the scalable manufacturing of high-efficiency tandem photovoltaics.

4 | Materials

[2-(9H-carbazol-9-yl)ethyl]phosphonic acid (TCI, CAS: 20999-38-6), 4-(3,6-diphenyl-9H-carbazol-9-yl)butyl)phosphonic acid (Suzhou LiWei Tech Co., Ltd, CAS: 2814500-04-2), lead iodide (TCI, 99.99%, trace metals basis, CAS: 10101-63-0), formamidinium iodide (Greatcell Solar Materials, CAS: 879643-71-7), formamidinium bromide (Dyenamo, CAS: 146958-06-7), methylammonium chloride (Dyenamo, CAS: 593-51-1), cesium chloride (TCI, ≥99.0%, CAS: 7647-17-8), fullerene-C_{60} (Sigma–Aldrich, CAS: 99685-96-8), bathocuproine (Lumtec, CAS: 4733-39-5), n-butylammonium iodide (Greatcell Solar Materials, CAS: 36945-08-1), propane-1,3-diammonium iodide (Greatcell Solar Materials, CAS: 120675-53-8), ethanol absolute anhydrous, ≥99.8% (VWR Chemicals, CAS: 64-17-5), 2-propanol, ≤ 0,003% water (VWR Chemicals, CAS: 67-63-0), methanol, anhydrous, ≥99.9% (VWR Chemicals, CAS: 67-56-1)

4.1 | Fabrication

Perovskite solar cell fabrication: Single-junction perovskite solar cells (PSCs) were fabricated on pre-patterned indium tin oxide

(ITO)-coated glass substrates (120 nm, 15 Ω sq^{-1}, Luminescence Technology Corp., Lumtec). The substrates were cleaned by sequential ultrasonication in acetone and isopropyl alcohol (IPA) (15 min each), dried with a nitrogen gun, and treated with oxygen plasma (100% O_2, 15 min) to remove residual contaminants and enhance surface wettability. For the HTL of the reference PSCs, a 2PACz solution (0.5 mg mL^{-1} in ethanol) was prepared one week in advance and sonicated for 60 min after preparation and again immediately prior to use. Inside a nitrogen-filled glovebox, 80 µL of this solution was spin-coated at 3000 rpm (1000 rpm s^{-1} acceleration) for 30 s, followed by annealing at 100°C for 10 min. To improve monolayer homogeneity, the films were rinsed by spin-coating ethanol under identical conditions and annealed again at 100°C for 10 min. For dip-coated SAM formation, the solution was fabricated identically but using different molarities. Up to seven substrates were dip-coated simultaneously in a beaker using a custom-built holder. After deposition, the samples were annealed identically to the spin-coated references and subsequently immersed in pure ethanol (60 s), followed by an annealing step, to remove excess molecules. Following HTL formation, the substrates were transferred to a thermal evaporation chamber, where inorganic precursor materials of CsCl (30 nm, 0.1 Å s^{-1}) and PbI_2 (300 nm, 1 Å s^{-1}) were sequentially deposited. The organic precursor ink consisted of FAI (35.27 mg mL^{-1}), FABr (30.64 mg mL^{-1}), and MACl (9 mg mL^{-1}) dissolved in IPA, with complete dissolution assisted by vortex mixing. This formulation corresponds to a nominal perovskite composition of $Cs_{0.18}FA_{0.63}MA_{0.19}Pb(I_{0.76}Br_{0.12}Cl_{0.12})_3$. Stoichiometric calculations assumed an ABX_3 lattice with PbI_2 as the sole B-site source. The required molar conversion was derived from the PbI_2 density (6.16 g cm^{-3}) and the deposited thickness of 300 nm, allowing determination of the A-site and halide ratios from the precursor masses and molar weights. The organic precursor was deposited using a PiXDRO LP50 inkjet printer equipped with a Sapphire QS-256/10 AAA printhead (10 pL nominal drop volume). The waveform parameters (width 9 µs, space 5.7 µs, level 45.88 V, rise/fall 64.7 V $µs^{-1}$) produced droplets of approximately 10 pL. Prior to printing, the evaporated inorganic thin films were removed from the nitrogen atmosphere. Both the vertical (printhead travel direction) and horizontal (perpendicular to printhead travel) step sizes were set to 8. The printhead remained in its native orientation throughout the printing process. Across multiple fabrication runs, a printing resolution of around 800 dots per inch (DPI) yielded the best film quality and device performance. After printing, the samples were annealed in ambient air (20°C, 40%–45% relative humidity) at 150°C for 15 min to complete perovskite conversion and were then returned to the glovebox [35]. For surface passivation, a 1 mg mL^{-1} $PDAI_2$ solution in IPA was prepared by sonication or shaking for 24 h, while a separate 1 mg mL^{-1} BAI solution in IPA was mixed for 5 min using a vortex shaker. The two solutions were combined and shook for an additional 5 min prior to use. In reference PSCs, the mixture was spin-coated onto the perovskite layer at 4000 rpm (1000 rpm s^{-1} acceleration) for 30 s, followed by annealing at 100°C for 5 min to remove residual solvent. For dip-coating passivated devices, the same custom dip-coating setup used for SAM deposition was employed, with adjusted molarities but otherwise identical preparation and annealing. Subsequently, the electron-transport layer consisting of C_{60} (20 nm, 0.2 Å s^{-1}) and bathocuproine (BCP, 3.5 nm, 0.2 Å s^{-1}) was thermally evaporated in sequence. After evaporation, to re-expose the ITO contact excess material was mechanically removed with a scalpel. Finally, 100 nm of Ag was deposited at 1 Å s^{-1} through a shadow mask, defining four individual PSCs with an active area of 10.5 mm^2 per substrate.

Perovskite module: The perovskite mini-module was fabricated using the same fully scalable, dip-coating-based process as the single PSCs but included three laser-scribing steps to form nine series-connected sub-cells. The P1 scribe was applied prior to HTL deposition, P2 before electrode formation, and P3 after electrode deposition, following the process described by Ritzer and Abzieher et al. [43].

Perovskite/silicon tandem solar cell fabrication: Commercial heterojunction silicon (HJT) bottom cells from Jiaxing Dazhe Solar Energy Co., Ltd. were used as substrates for the perovskite/silicon tandems (PSTs). These were based on n-type diamond-wire-sawn monocrystalline silicon wafers (half-cut G12 format, 210 × 105 mm^2, 220 ± 2 µm thickness, 0.8 ± 0.1 Ω cm resistivity). Wafer pretreatment involved alkaline etching to remove saw damage, followed by surface texturing and polishing to reduce reflectance, and RCA cleaning to eliminate residual contamination. The heterojunction structure was formed in a 13.56 MHz PECVD system at 190°C by depositing an intrinsic a-Si:H passivation layer (8 ± 1 nm) on both sides, followed by an n-type µc-SiO_x:H layer (20 ± 1 nm) on the front and a p-type µc-Si:H layer on the rear, yielding a total rear stack thickness of 25 ± 1 nm. Transparent conductive oxide layers were then sputtered using a rotating In_2O_3:SnO_2 (99:1) ceramic target, resulting in 100 nm ITO on the p-side and 10 nm ITO on the n-side. Metallization was completed by screen printing and sintering at 210 ± 5°C. Before perovskite deposition, the silicon solar cells were annealed at 200°C for 20 min in a nitrogen glovebox and dynamically spin-coated with acetone and IPA at 2500 rpm for 30 s (1000 rpm s^{-1} acceleration), followed by drying at 100°C for 10 min. Next, a 10 nm nickel oxide layer was sputter-deposited from a target at 100 W using pure argon at a pressure of 1 mTorr. Subsequently, Ph4PACz (prepared at the same molarity as the 2PACz reference solution, but in methanol) was deposited by dip-coating for 60 s after at least 3 h of sonication to ensure complete dissolution. After dip-coating, the substrates were annealed at 100°C for 10 min, rinsed by a second dip-coating step in pure methanol to remove excess material, and finally dried again at 100°C for 10 min. The perovskite absorber was then deposited using the same hybrid two-step evaporation/inkjet-printing process route described for the single-junction PSCs. After crystallization, $PDAI_2$-BAI passivation was applied using dip-coating. The ETL comprised 20 nm of thermally evaporated C_{60}, followed by a 20 nm SnO_2 layer grown by reactive ALD using tetrakis(dimethylamino)tin(IV) and water as precursors (TDMASn pulse 1.6 s with 12 s purge and H_2O pulse 0.1 s with 16 s purge. N_2 was used as carrier gas with 99.999% purity). The TDMASn source was preheated to 70°C for 1 h to ensure stable conditions. A 45 nm indium zinc oxide (IZO) top electrode was sputtered at 1 mTorr using 190 W power in Ar/O_2. atmosphere. The active area (1 cm^2) was defined using a shadow mask. Silver front contacts (600 nm) were thermally evaporated, incorporating six 100 µm-wide fingers extending partially into the active region to enhance charge extraction. Finally, a 110 nm MgF_2 antireflection coating was deposited. Reported thicknesses

on textured substrates represent nominal values obtained from quartz crystal microbalance readings. The effective thickness may be reduced due to the increased surface area of the texture.

5 | Characterization

5.1 | *JV* Measurements

The *JV* measurements of the single-junction PSCs were recorded using a xenon-lamp solar simulator (Newport Oriel Sol3A) providing an AM1.5G spectrum at an irradiance of 1000 W m^{-2}. The illumination intensity was calibrated with a certified silicon reference solar cell (Newport) equipped with a KG5 filter. PSCs were scanned in both forward and reverse directions with a voltage increment of 10 mV over a range of −0.2–1.3 V at a scan rate of 0.6 V s^{-1}, controlled by a Keithley 2401 source meter. During the measurements, the sample temperature was maintained at 25°C using a microcontroller-regulated Peltier stage. All PSC measurements were carried out inside a nitrogen-filled glovebox. For PSTs, a pre-calibrated LED solar simulator (Sinus-70 Advanced, WAVELABS Solar Metrology Systems GmbH) was employed under ambient conditions. The voltage range was −0.2–2.0 V using a Keithley 2400 unit. Long-term MPP tracking was conducted with an LED solar simulator (PR-LEDSUN-22R, PURI Materials), applying a perturb-and-observe algorithm. Due to the use of a multi-substrate holder and a measurement position slightly off-center, the light intensity during long-term MPP tracking was marginally reduced. During PST characterization, the illuminated area was set to 1 cm^2 using an aperture mask.

5.2 | External Quantum Efficiency Measurements

External quantum efficiency (EQE) measurements were conducted using a QE-R system (RR01240806, EnliTech) under ambient conditions. For tandem devices, sub-cell-selective characterization was achieved by applying appropriate bias illumination and bias voltages. A near-infrared bias light (940 nm), together with an optimized bias voltage, was used to measure the perovskite top cell, whereas a blue bias light (450 nm) and the corresponding bias voltage were employed for the silicon bottom cell. The measurements were performed at a chopping frequency of 210 Hz.

5.3 | Time-Resolved Photoluminescence Measurements

Time-resolved photoluminescence (TRPL) measurements were performed on a commercial fluorescence spectrometer (Edinburgh Instruments FLS920) by time-correlated single-photon counting (TCSPC). For excitation, a 635 nm picosecond pulsed laser (Picoquant LDH-series) operating at 50 kHz repetition rate and a power of 1.7 μW at the sample position was used. The laser was focused to a spot size of ∼ 0.3 mm diameter, resulting in an excitation density of ∼ $1.5{\cdot}10^6$ photons cm^{-2}. The detection monochromator was set to 750 nm central wavelength with a width of 2 nm. For carrier lifetime determination the transients were fitted using a triple-exponential decay model and subsequently taking the amplitude averaged lifetime from the fit results.

5.4 | Scanning Electron Microscopy

Scanning electron microscopy (SEM) was carried out with a Zeiss LEO1530 SEM operated with an in-lens detector. Aperture sizes between 20 and 30 μm were used, and acceleration voltages of 3–5 kV were applied.

5.5 | Kelvin Probe Force Microscopy

Kelvin probe force microscopy (KPFM) measurements were performed in frequency modulation (FM) mode using a Bruker system. Images were acquired in lift-mode over an area of 500 nm × 500 nm with a resolution of 128 × 128 pixels. The scan rate was set to 0.2 Hz, with a tip velocity of 0.1 μm s^{-1} and a lift height of 200 nm. Interleaved FM-KPFM feedback was enabled to monitor the surface potential, and all measurements were conducted in nitrogen atmosphere.

5.6 | Ultraviolet Photoelectron Spectroscopy

Ultraviolet photoelectron spectroscopy (UPS) was performed with an ESCALAB XI+ instrument (Thermo Fisher), utilizing a He(1) source (21.22 eV) under 0 V and −5.0 V bias.

5.7 | X-Ray Photoelectron Spectroscopy

X-ray photoelectron spectroscopy (XPS) was conducted using a K-Alpha instrument (Thermo Scientific), equipped with a monochromatic Al Kα X-ray Omicron XM1000 X-ray source (hf = 1486.6 eV), referencing the binding energy scale to the C 1*s* signal.

5.8 | Photoluminescence & k-Mapping

To perform photoluminescence and k-mapping measurements, two 467 nm LED bars (LDL2-170/30-BL2, Creating Customer Satisfaction Inc.) were used as excitation sources in a symmetrical 45° configuration and powered by a control unit (PD3-5024-4-EI, Creating Customer Satisfaction Inc.). The emitted signal was recorded using an sCMOS camera (CS2100M-USB – Quantalux 2.1 MP Monochrome sCMOS Camera, Thorlabs) equipped with a macro zoom lens (Zoom 7000, Navitar) and operated with an exposure time of 50 ms. To suppress detection of the excitation light, a 695 nm absorptive long-pass filter (092 MRCIR – M55.0×0.75, Schneider-Kreuznach) was mounted on the lens. Spatially resolved photoluminescence (I_{PL}) measurements were conducted over an excitation intensity range (I_{exc}) of 0.005-0.2 suns, including a background correction acquired at zero excitation. The parameter k was determined as the exponent obtained from fitting the power-law model $I_{PL} \sim {I_{exc}}^{k}$, to the excitation-intensity-dependent photoluminescence images on a pixel-by-pixel basis [39]. This parameter k, also known as the "optical ideality factor", provides insight into the dominant

recombination mechanisms and thereby into the quality of the thin film.

5.9 | Statistical Representation

In the boxplots, graphical elements are used to convey key statistical information. The colored boxes indicate the interquartile range (IQR), spanning from the 25th to the 75th percentile. Whiskers extend to 1.5 times the IQR to help identify potential outliers. The horizontal line inside the box marks the median, while the hollow square represents the mean. Individual data points, including outliers, are shown separately.

Author Contributions

R.P., **L.P.R.**, **J.S.**, **U.L.**, and **U.W.P.** conceived the idea and designed the experiments. **R.P.**, **L.P.R.**, **J.S.**, **L.F.**, **T.K.**, **J.P.**, **U.K.D.**, **R.T.**, **D.B.R.**, **T.P.**, **D.O.B.**, **M.G.**, and **T.Z.** fabricated PSCs and PSTs, characterized them, and analyzed the data. **J.L.**, **U.L.**, and **U.W.P.** supervised the project. All authors were involved in the discussions and contributed to writing the manuscript.

Acknowledgements

Financial support by the Initiating and Networking funding of the Helmholtz Association, the Solar Technology Acceleration Platform (Solar TAP) and Project Zeitenwende ("accelerated transfer of the next generation of solar cells to mass production"), the program-oriented funding IV of the Helmholtz Association (Materials and Technologies for the Energy Transition, Topic 1: Photovoltaics and Wind Energy, Code: 38.01.04), the German Federal Ministry of Economic Affairs and Energy (BMWE) through the project TIPSTAR (03EE1199B) and HYPER (03EE1222B), the Max Planck School of Photonics (MPSP) supported by the German Federal Ministry of Education and Research (BMBF), the Max Planck Society, and the Fraunhofer Society is gratefully acknowledged. The authors also gratefully acknowledge support from the Karlsruhe Nano Micro Facility (KNMF), the Karlsruhe School of Optics & Photonics (KSOP) and thank the whole "perovskite task force" and "MNOS group" at KIT for fruitful discussions and assistance. We acknowledge the developers of KI-Toolbox, which is an internal AI assistant from Karlsruhe Institute of Technology, that was used to polish the English language. The first author expresses gratitude to Benedikt Liebmann for the support regarding the design of the Blender-based 3D representations.

Open access funding enabled and organized by Projekt DEAL.

Conflicts of Interest

The authors declare no conflicts of interest.

Data Availability Statement

The data that support the findings of this study are available from the corresponding author upon reasonable request.

References

1. G. Yang, C. Deng, C. Li, et al., "Towards Efficient, Scalable and Stable Perovskite/Silicon Tandem Solar Cells," *Nature Photonics* 19 (2025): 913–924.

2. E. Aydin, T. G. Allen, M. De Bastiani, et al., "Pathways Toward Commercial Perovskite/Silicon Tandem Photovoltaics," *Science* 383 (2024): adh3849.

3. L. Zhang, M. Zhang, H. Wang, et al., "Diverse Perovskite Solar Cells: Progress, Challenges, and Perspectives," *Advanced Materials* 38 (2026): 12221.

4. H. Li, J. Zhou, L. Tan, et al., "Sequential Vacuum-Evaporated Perovskite Solar Cells with More Than 24% Efficiency," *Science Advances* 8 (2022): 7422.

5. I. Gomar-Fernández, L. Gil-Escrig, N. Rodkey, et al., "Large-Area Close-Space Sublimation Enables the Fabrication of Efficient and Stable Perovskite Solar Cells," *EES Solar* 1 (2025): 1126–1134.

6. T. Feeney, J. Petry, A. Torche, et al., "Understanding and Exploiting Interfacial Interactions Between Phosphonic Acid Functional Groups and Co-Evaporated Perovskites," *Matter* 7 (2024): 2066–2090.

7. K. Geistert, R. Pappenberger, P. Scharfer, et al., "Spatially Regulated Gas Flow Control for Batch-Drying of Large Area Slot-Die-Coated Perovskite Thin Films," *Advanced Energy Materials* 15 (2025): 2500923.

8. I. Zimmermann, M. Al Atem, O. Fournier, et al., "Sequentially Slot-Die-Coated Perovskite for Efficient and Scalable Solar Cells," *Advanced Materials Interfaces* 8 (2021): 2100743.

9. O. Er-Raji, A. A. Said, A. S. Subbiah, et al., "Coating Dynamics in Two-Step Hybrid Evaporated/Blade-Coated Perovskites for Scalable Fully-Textured Perovskite/Silicon Tandem Solar Cells," *EES Solar* 1 (2025): 419–430.

10. H. Fang, W. Shen, H. Guan, et al., "Efficient Blade-Coated Wide-Bandgap and Tandem Perovskite Solar Cells via a Three-Step Restraining Strategy," *Advanced Materials* 37 (2025): 2414790.

11. U. K. Dangudubiyyam, R. Pesch, O. Karakaya, et al., "Eco-Friendly Solvent System for Inkjet Deposition of Wide Bandgap Perovskite Solar Cells Enabling Tandem Integration," *Advanced Science* (2026): 76463.

12. V. V. Satale, S. Chowdhury, A. Mohamed, et al., "Green Solvent Enabled Perovskite Ink for Ambient-Air-Processed Efficient Inkjet-Printed Perovskite Solar Cells," *Advanced Functional Materials* 35 (2025): 2503717.

13. H. Cai, X. Liang, X. Ye, et al., "High Efficiency Over 20% of Perovskite Solar Cells by Spray Coating via a Simple Process," *ACS Applied Energy Materials* 3 (2020): 9696–9702.

14. M. V. Kelso, N. K. Mahenderkar, Q. Chen, J. Z. Tubbesing, and J. A. Switzer, "Spin Coating Epitaxial Films," *Science* 364 (1979): 166–169.

15. L. Fang, M. Ren, B. Li, et al., "Interfacial Design Strategies for Stable and High-Performance Perovskite/Silicon Tandem Solar Cells on Industrial Silicon Cells," *Nature Communications* 16 (2025): 8881.

16. X. Liu, M. Rienäcker, M. Gholipoor, et al., "Charge Carrier Management for Highly Efficient Perovskite/Si Tandem Solar Cells with Poly-Si Based Passivating Contacts," *Energy & Environmental Science* 18 (2025): 5599–5609.

17. X. Y. Chin, D. Turkay, J. A. Steele, et al., "Interface Passivation for 31.25%-efficient Perovskite/Silicon Tandem Solar Cells," *Science* 381 (1979): 59–63.

18. O. Er-Raji, C. Messmer, R. R. Pradhan, et al., "Electron Accumulation Across the Perovskite Layer Enhances Tandem Solar Cells with Textured Silicon," *Science* 390 (1979): adx1745.

19. Y. Jin, H. Feng, Y. Li, et al., "Recrystallizing Sputtered NiOx for Improved Hole Extraction in Perovskite/Silicon Tandem Solar Cells," *Advanced Energy Materials* 15 (2025): 2403911.

20. R. Pappenberger, R. Singh, A. Diercks, et al., "Versatile Two-Step Process for Perovskite-Based Tandem Photovoltaics," *Solar RRL* 9 (2025): 2500193.

21. M. Piot, L. Gil-Escrig, F. Ventosinos, et al., "Vacuum Deposition of Triple-Halide Wide-Bandgap Perovskites Enabled by Sublimation of Mixed Organic-Halide Pellets," *ACS Materials Letters* 7 (2025): 3692–3698.

22. D. Grosso, "How to Exploit the Full Potential of the Dip-coating Process to Better Control Film Formation," *Journal of Materials Chemistry* 21 (2011): 17033–17038.

23. P. J. Hotchkiss, S. C. Jones, S. A. Paniagua, et al., "The Modification of Indium Tin Oxide with Phosphonic Acids: Mechanism of Binding, Tuning of Surface Properties, and Potential for Use in Organic Electronic Applications," *Accounts of Chemical Research* 45 (2012): 337–346.

24. L. Xiang, X. Yang, X. Liu, et al., "Dip-Coating of Self-Assembled Monolayers for Perovskite Photovoltaic Applications," *EcoEnergy* 3 (2025): 70007.

25. A. Ulman, "Formation and Structure of Self-Assembled Monolayers," *Chemical Reviews* 96 (1996): 1533–1554.

26. F. Schreiber, "Structure and Growth of Self-Assembling Monolayers," *Progress in Surface Science* 65 (2000): 151–257.

27. A. Magomedov, A. Al-Ashouri, E. Kasparavicius, et al., "Self-Assembled Hole Transporting Monolayer for Highly Efficient Perovskite Solar Cells," *Advanced Energy Materials* 8 (2018): 1801892.

28. F. Sahli, J. Werner, B. A. Kamino, et al., "Fully Textured Monolithic Perovskite/Silicon Tandem Solar Cells with 25.2% Power Conversion Efficiency," *Nature Materials* 17 (2018): 820–826.

29. O. Er-raji, M. A. A. Mahmoud, O. Fischer, et al., "Tailoring Perovskite Crystallization and Interfacial Passivation in Efficient, Fully Textured Perovskite Silicon Tandem Solar Cells," *Joule* 8 (2024): 2811–2833.

30. C. Liu, Y. Yang, H. Chen, et al., "Bimolecularly Passivated Interface Enables Efficient and Stable Inverted Perovskite Solar Cells," *Science* 382 (1979): 810–815.

31. H. Chen, A. Maxwell, C. Li, et al., "Regulating Surface Potential Maximizes Voltage in All-Perovskite Tandems," *Nature* 613 (2023): 676–681.

32. K. Zhang, A. Vincze, E. Metwalli, et al., "Impact of 2D Ligands on Lattice Strain and Energy Losses in Narrow-Bandgap Lead–Tin Perovskite Solar Cells," *Advanced Functional Materials* 33 (2023): 2303455.

33. A. Al-Ashouri, A. Magomedov, M. Roß, et al., "Conformal Monolayer Contacts with Lossless Interfaces for Perovskite Single Junction and Monolithic Tandem Solar Cells," *Energy & Environmental Science* 12 (2019): 3356–3369.

34. R. Pesch, A. Diercks, J. Petry, et al., "Hybrid Two-Step Inkjet-Printed Perovskite Solar Cells," *Solar RRL* 8 (2024): 2400165.

35. R. Pesch, J. Petry, J. Petermann, et al., "Efficient Perovskite/Silicon Tandem Solar Cells Using Hybrid Two-Step Inkjet Printing with Edge Isolation Precision," *Small Science* 5 (2025): 2500362.

36. V. Yeddu, K. Almasabi, Y. Xu, et al., "In-Situ Self-Assembly of Hole Transport Monolayer During Crystallization for Efficient Single-Crystal Perovskite Solar Cells," *Nature Communications* 16 (2025): 7245.

37. G. Qu, S. Cai, Y. Tao, et al., "A Self-Assembled Monolayer via Rapid and Scalable Soak Coating for Perovskite Solar Cells," *Nature Synthesis* (2026).

38. M. Abdi-Jalebi, Z. Andaji-Garmaroudi, S. Cacovich, et al., "Maximizing and Stabilizing Luminescence From Halide Perovskites with Potassium Passivation," *Nature* 555 (2018): 497–501.

39. B. Hacene, F. Laufer, S. Ternes, et al., "Intensity Dependent Photoluminescence Imaging for In-Line Quality Control of Perovskite Thin Film Processing," *Advanced Materials Technologies* 9 (2024): 2301279.

40. L. Tan, J. Zhou, X. Zhao, et al., "Combined Vacuum Evaporation and Solution Process for High-Efficiency Large-Area Perovskite Solar Cells With Exceptional Reproducibility," *Advanced Materials* 35 (2023): 2205027.

41. S. Pisoni, F. Fu, R. Widmer, et al., "Impact of Interlayer Application on Band Bending for Improved Electron Extraction for Efficient Flexible Perovskite Mini-modules," *Nano Energy* 49 (2018): 300–307.

42. T. Yu, M. Zhang, Y. Jiang, et al., "A Two-Step Hybrid Evaporation-Solution Method for Fabricating Large-Area High-Efficiency Perovskite Solar Cells," *Organic Electronics* 152 (2026): 107400.

43. D. B. Ritzer, T. Abzieher, A. Basibüyük, et al., "Upscaling of Perovskite Solar Modules: The Synergy of Fully Evaporated Layer Fabrication and All-Laser-Scribed Interconnections," *Progress in Photovoltaics: Research and Applications* 30 (2022): 360–373.

44. A. Sun, C. Tian, R. Zhuang, et al., "High Open-Circuit Voltage (1.197 V) in Large-Area (1 cm^2) Inverted Perovskite Solar Cell via Interface Planarization and Highly Polar Self-Assembled Monolayer," *Advanced Energy Materials* 14 (2024): 2303941.

45. H. Luo, X. Zheng, W. Kong, et al., "Inorganic Framework Composition Engineering for Scalable Fabrication of Perovskite/Silicon Tandem Solar Cells," *ACS Energy Letters* 8 (2023): 4993–5002.

46. X. Zheng, W. Kong, J. Wen, et al., "Solvent Engineering for Scalable Fabrication of Perovskite/Silicon Tandem Solar Cells in Air," *Nature Communications* 15 (2024): 4907.

47. Z. Liu, S. Yang, Y. Tian, et al., "Homogeneity Regulation in Sequential Fabricated Perovskite Film for Industrial-Scale Deposition of Fully-Textured Perovskite/Silicon Tandem Cells," *Advanced Materials* 38 (2026): 11177.

48. J. Petry, R. Pappenberger, A. Welle, et al., "Benchmarking Inorganic Deposition Routes for Hybrid Two-Step Processed Perovskite Solar Cells: A Materials Perspective," *Solar RRL* 10 (2026): 202500698.

49. D. Zhang, T. Wu, B. Li, et al., "Iceberg-Like Pyramids in Industrially Textured Silicon Enabled 33% Efficient Perovskite-Silicon Tandem Solar Cells," *Nature Communications* 16 (2025): 7331.

50. J. Thiesbrummel, S. Shah, E. Gutierrez-Partida, et al., "Ion-Induced Field Screening as a Dominant Factor in Perovskite Solar Cell Operational Stability," *Nature Energy* 9 (2024): 664–676.

51. M. V. Khenkin, E. A. Katz, A. Abate, et al., "Consensus Statement for Stability Assessment and Reporting for Perovskite Photovoltaics Based on ISOS Procedures," *Nature Energy* 5 (2020): 35–49.

Supporting Information

Additional supporting information can be found online in the Supporting Information section.

Supporting File: aenm71579-sup-0001-SuppMat.pdf.